The Astrophysical Journal Letters, 722:L39–L44, 2010 October 10 doi:10.1088/2041-8205/722/1/L39

EVIDENCE FOR GAMMA-RAY HALOS AROUND ACTIVE GALACTIC NUCLEI AND THE FIRST MEASUREMENT OF INTERGALACTIC MAGNETIC FIELDS

Shin'ichiro Ando[1] and Alexander Kusenko[2,3]
[1] California Institute of Technology, Mail Code 350-17, Pasadena, CA 91125, USA; ando@caltech.edu
[2] Department of Physics & Astronomy, University of California, Los Angeles, CA 90095, USA
[3] Institute for the Physics & Mathematics of the Universe, University of Tokyo, Kashiwa, Chiba 277-8568, Japan; kusenko@ucla.edu
Received 2010 June 10; accepted 2010 September 1; published 2010 September 17

ABSTRACT

Intergalactic magnetic fields (IGMFs) can cause the appearance of halos around the gamma-ray images of distant objects because an electromagnetic cascade initiated by a high-energy gamma-ray interaction with the photon background is broadened by magnetic deflections. We report evidence of such gamma-ray halos in the stacked images of the 170 brightest active galactic nuclei (AGNs) in the 11 month source catalog of the *Fermi Gamma-Ray Space Telescope*. Excess over the point-spread function in the surface brightness profile is statistically significant at 3.5σ (99.95% confidence level), for the nearby, hard population of AGNs. The halo size and brightness are consistent with IGMF, $B_{\rm IGMF} \approx 10^{-15}$ G. The knowledge of IGMF will facilitate the future gamma-ray and charged-particle astronomy. Furthermore, since IGMFs are likely to originate from the primordial seed fields created shortly after the big bang, this potentially opens a new window on the origin of cosmological magnetic fields, inflation, and the phase transitions in the early universe.

Key words: galaxies: active – gamma rays: general – ISM: magnetic fields

Online-only material: color figures

1. INTRODUCTION

Intergalactic magnetic fields (IGMFs) had not been measured until now, despite their importance for gamma-ray and cosmic-ray astronomy and their likely connection to the primordial fields that could have seeded the stronger magnetic fields observed in galaxies, Sun, and Earth. This is because IGMFs are too small for conventional astronomical probes such as Zeeman splitting or Faraday rotation. Unlike the fields in galaxies, which are believed to have been amplified by the dynamo action of the large-scale convective motions of gas, the fields in voids remain low, close to their primordial values modified only by the relatively small contribution of the fields leaking out of galaxies (Kronberg 1994; Grasso & Rubinstein 2001; Widrow 2002; Kulsrud & Zweibel 2008). The observational and theoretical upper bounds on IGMFs constrain their magnitudes to be below 10^{-9} G (Barrow et al. 1997), whereas any value above $\sim 10^{-30}$ G is sufficient to explain the $\sim\mu$G Galactic magnetic fields' generation by the dynamo mechanism (Davis et al. 1999).

One can detect such extremely weak fields using high-energy gamma rays (Aharonian et al. 1994; Plaga 1995). Very energetic photons emitted from active galactic nuclei (AGNs) or other strong sources produce pairs of electrons and positrons in their interactions with the extragalactic background light (EBL). These pairs upscatter the cosmic microwave background photons to high energies, giving rise to an electromagnetic cascade, and the photons from the cascade are detected by gamma-ray telescopes such as *Fermi*. Since the trajectories of electrons and positrons in the cascade are affected by magnetic fields, a gamma-ray image of AGNs is expected to exhibit a halo of secondary photons around a bright central point-like source (Aharonian et al. 1994; Dolag et al. 2009; Neronov & Semikoz 2009). The central image is expected to be composed of photons emitted directly from the source with energies below the pair production threshold. In addition, delays in arrival times of the secondary photons can be used to probe IGMFs (Plaga 1995; Ando 2004; Murase et al. 2008). Finally, at TeV energies, the secondary photons produced in interactions of cosmic rays with EBL may have already been observed by the air Cherenkov telescopes (Essey & Kusenko 2010; Essey et al. 2010).

Thus far, in TeV range, HEGRA (Aharonian et al. 2001) and MAGIC (Aleksic et al. 2010) did not detect any halo component of two bright blazars, Mrk 501 and Mrk 421, and they set upper limits on the flux. In particular, the analysis of MAGIC using gamma rays above 300 GeV excludes some range of IGMFs between 4×10^{-15} and 10^{-14} G. Very recently, IGMFs above 3×10^{-16} G were proposed as an explanation of non-observation by *Fermi* of several AGNs known to be bright TeV sources (Neronov & Vovk 2010; see also Tavecchio et al. 2010).

In this Letter, we present evidence of extended images and of IGMFs at 3.5σ level, based on gamma-ray data collected by the Large Area Telescope (LAT) on board *Fermi*, in the energy range between 1 GeV and 100 GeV. It is consistent with pair-halo scenario with IGMF, $B_{\rm IGMF} \approx 10^{-15}$ G. The knowledge on IGMF will facilitate the future gamma-ray and cosmic-ray astronomy, and it will open a new window on the origin of cosmological magnetic fields (Cornwall 1997), inflation (Turner & Widrow 1988; Diaz-Gil et al. 2008), and the phase transitions in the early universe (Vachaspati 1991, 2001; Baym et al. 1996).

2. STACKED GAMMA-RAY IMAGES OF AGNs

The individual photon data as well as the 11 month source catalog (Abdo et al. 2010a) are now publicly available.[4] Among ~700 AGNs in the *Fermi* AGN catalog (Abdo et al. 2010b), we select 170 AGNs that are detected at more than 4.1σ in the highest-energy band, 10–100 GeV, and located at high Galactic latitudes, $|b| > 10^\circ$. These sources are likely to have a hard spectrum and produce a large number of TeV primary photons, which is necessary for the appearance of the secondary halo. Although each individual AGN produces too few photon counts, especially in the highest-energy band, one can dramatically improve the statistics by stacking all of these 170 AGN

[4] http://fermi.gsfc.nasa.gov/ssc/

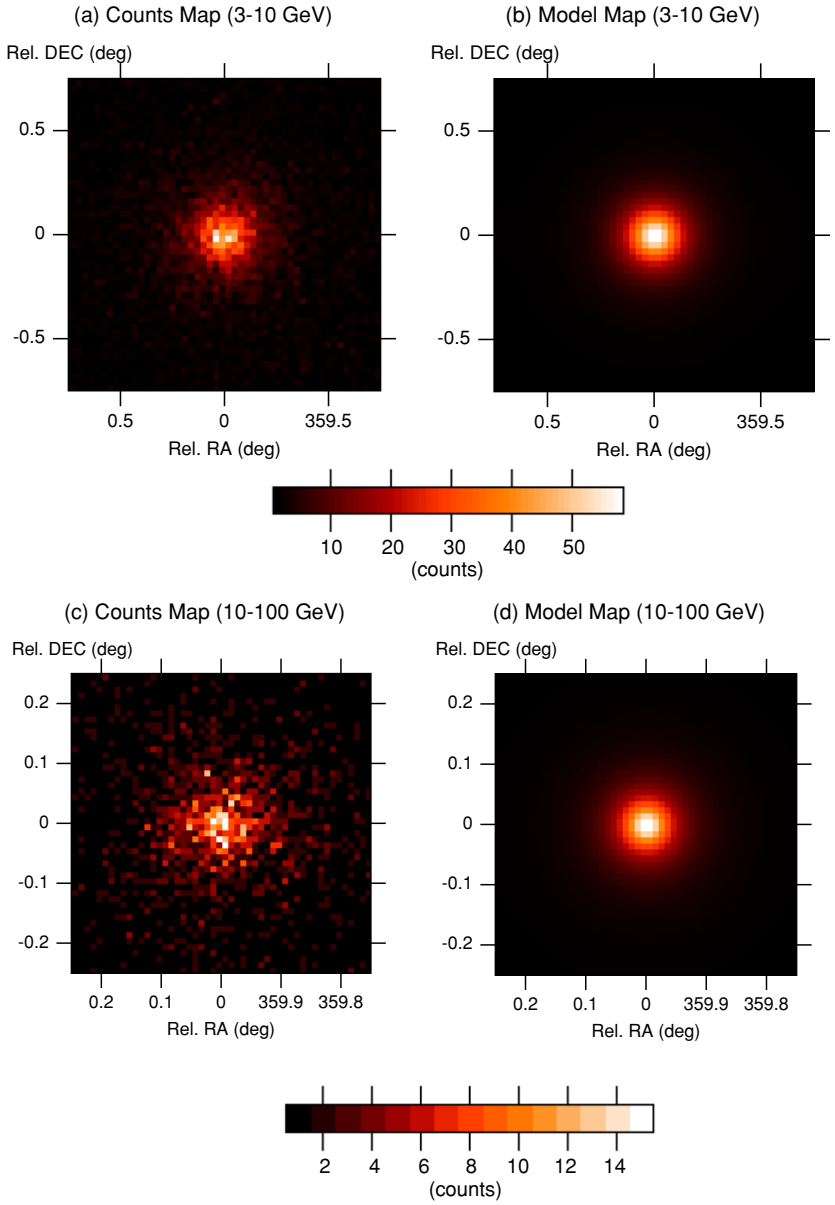

Figure 1. Gamma-ray counts and point-source model maps of stacked 170 bright AGNs. Upper and lower panels are for 3–10 GeV ((a) and (b)) and 10–100 GeV ((c) and (d)) bands, respectively. Left panels ((a) and (c)) are the actual data counts of stacked 170 AGNs, and the right panels ((b) and (d)) show the "best-fit" point-source model (including backgrounds). Pixel size is $0.^{\circ}03$ ($0.^{\circ}01$) for the 3–10 (10–100) GeV band.

(A color version of this figure is available in the online journal.)

maps. We perform the analysis in three separate energy bands: 1–3 GeV, 3–10 GeV, and 10–100 GeV, which allows us to study the energy dependence of the halos. To obtain source and model maps, we use official *Science Tools* made publicly available by the *Fermi* team. The photons that we use in the AGN analysis are collected between 239,557,417 s and 268,416,079 s in the mission elapsed time (MET), and they are of "Diffuse" class.

We use locations of AGNs from the 11 month source catalog, i.e., those obtained solely by the gamma-ray data. This does not introduce any significant uncertainty of the stacked images, because the localization accuracy using gamma rays is typically much better than the size of point-spread function (PSF), especially for hard AGN (Abdo et al. 2010b).

Figure 1 shows the gamma-ray count maps of stacked 170 AGNs and the "best-fit" point-source model generated with the *Fermi Science Tools* as well as point-source catalog, smeared only by the PSF of LAT (we use the latest "Pass6 version 3" instrument response function of LAT). It is evident that the counts map and the model map are not consistent with each other, especially in the 10–100 GeV range.

3. FLUX AND ANGULAR EXTENT OF HALO COMPONENT

We have performed maximum likelihood analysis assuming that, in addition to the central point sources and diffuse backgrounds (Strong et al. 2004; Abdo et al. 2009, 2010d), there is a third component, namely, the halo component, whose spatial extent is given by the Gaussian distribution:

$$P_{\rm halo}\left(\theta^2|\theta^2_{\rm halo}\right) = \frac{2}{\pi\theta^2_{\rm halo}} \exp\left(-\frac{\theta^4}{\pi\theta^4_{\rm halo}}\right), \qquad (1)$$

where θ is the angle from the map center and $\theta^2_{\rm halo}$ is the mean of θ^2 over this distribution function, $\theta^2_{\rm halo} \equiv \langle\theta^2\rangle$. We fit the histogram of photon counts as a function of θ^2 read from the maps by minimizing

$$\chi^2 = \sum_i \frac{1}{N_i}\left[N_{\rm psf}P_{\rm psf}(\theta_i^2) + N_{\rm halo}P_{\rm halo}(\theta_i^2|\theta^2_{\rm halo}) + N_{{\rm bg},i} - N_i\right]^2, \quad (2)$$

where $N_{\rm psf}$, $N_{\rm halo}$, and $\theta_{\rm halo}$ are treated as free parameters. The index i refers to the ith bin, N_i is the total number of events in this bin, $P_{\rm psf}$ is the normalized PSF, and $N_{{\rm bg},i}$ is the events due to diffuse backgrounds. We fix the backgrounds to the values at $\theta^2 = 2.025$–2.25 deg^2 and 0.233–0.25 deg^2 for 3–10 GeV and 10–100 GeV, respectively, in the simulated maps, assuming that they are homogeneous. Thus, $N_{\rm psf}$ and $N_{\rm halo}$ are the total numbers of photons in the map attributed to the point source and the halo, respectively, and $\theta_{\rm halo}$ is the apparent angular extent of the halo component.

The inclusion of the halo component improves the fit significantly at high energies. The minimum χ^2 over degree of freedom (ν) is $\chi^2_{\rm min}/\nu = 18.8/19$ and $13.3/12$ for 3–10 GeV and 10–100 GeV, respectively. In contrast, the "best-fit" point-source model, where $N_{\rm psf}$ and the background amplitude are treated as free parameters, gives $\chi^2_{\rm min}/\nu \simeq 66/20$ and $62/13$ for 3–10 GeV and 10–100 GeV, respectively. This clearly shows that, even though we stack many AGNs, this simple Gaussian halo model gives a very good fit to the data. The surface brightness profiles $dN/d\theta^2$ of the best-fit halo model are juxtaposed with the data points in Figure 2.

In Figure 3(a), we show the allowed regions of $\theta_{\rm halo}$ and $f_{\rm halo}$ at 68% and 95% confidence levels. Here, $f_{\rm halo}$ is the fraction of the halo photons, i.e., $f_{\rm halo} \equiv N_{\rm halo}/(N_{\rm psf} + N_{\rm halo})$. The best-fit values and 1σ statistical errors for these parameters are $\theta_{\rm halo} = 0.^\circ49 \pm 0.^\circ03$ and $f_{\rm halo} = 0.097 \pm 0.014$ for 3–10 GeV, and $\theta_{\rm halo} = 0.^\circ26 \pm 0.^\circ01$ and $f_{\rm halo} = 0.20 \pm 0.02$ for 10–100 GeV. For the lowest energy band, 1–3 GeV, only an upper limit on $f_{\rm halo}$ is obtained, which is $f_{\rm halo} < 0.046$ at 95% confidence level.

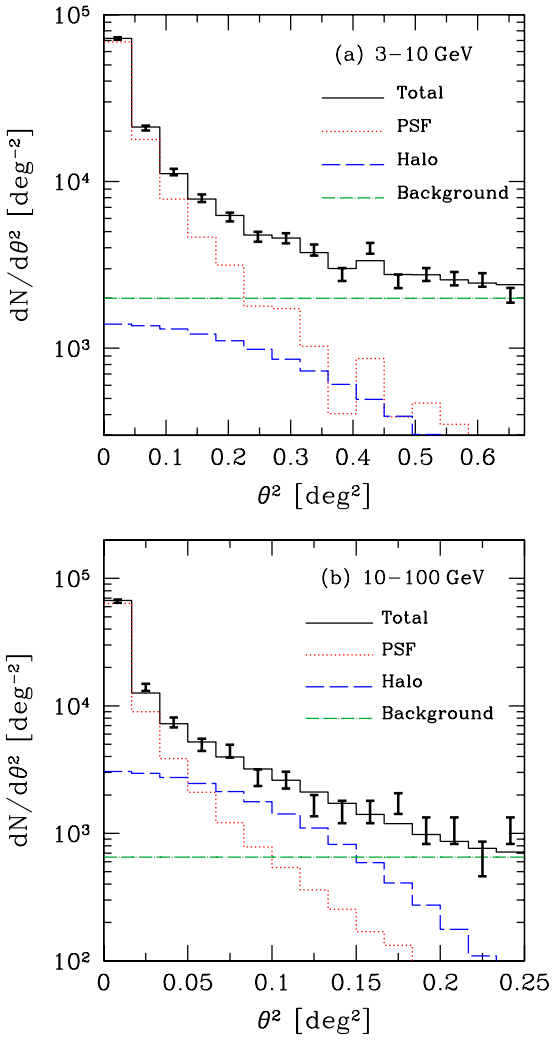

Figure 2. Surface brightness profile of the stacked gamma-ray images. Panels (a) and (b) are for 3–10 GeV and 10–100 GeV bands, respectively. Points with error bars are the data, and solid histogram is the best-fit model. The dotted, dashed, and dot-dashed histograms represent truly point-like source, halo component, and homogeneous diffuse background, respectively.

(A color version of this figure is available in the online journal.)

4. ELIMINATING INSTRUMENTAL EFFECTS

4.1. Dependence on Redshifts and Spectra

We discuss the possibility that these halos could be due to some unknown instrumental effect such as, for example, a possible deviation of LAT PSF from its value measured in calibration prior to the launch. To exclude such a possibility, we first consider samples of AGNs at different redshifts. We divide the 99 AGNs with known distances (out of total 170) into two groups: a sample of 57 nearby AGNs with $z < 0.5$ and a sample of 42 distant AGNs with $0.5 < z < 2.5$, where z is the redshift of the source. The allowed regions of $\theta_{\rm halo}$ and $f_{\rm halo}$ for these two samples, both for 3–10 GeV and 10–100 GeV, are shown in Figure 3(b). The statistically significant difference between the two populations shown in this figure implies that at least some component of the halos cannot be attributed to instrumental effects.

We also note that most AGNs in the nearby sample at $z < 0.5$ (53 among 57) are classified as the hardest population of gamma-ray blazars, BL Lac objects (Abdo et al. 2010b, 2010c). The distant sample, on the other hand, consists of 33 flat-spectrum radio quasars (and 9 others), which are known to be softer population. The fact that we measured the brighter and more extended additional components for the nearby/hard sample (Figure 3(b)) is consistent with the pair-halo scenario, because the harder AGN radiate more TeV photons that source secondary halos as well as they are closer. This cannot be easily understood as instrumental systematics, on the other hand, because the true PSF size would have to be an increasing function of energy, which is not the case; see discussions in the next subsection.

As another independent test to rule out instrumental effects, we considered a sample of 43 AGNs from the same catalog (Abdo et al. 2010a), which produced no photons above 10 GeV but were detected in the 3–10 GeV band at more than 4.1σ. These sources are likely to have a softer spectrum, with a negligible flux of primary photons above the pair production threshold. In the absence of pair production, one expects to see no halos. As expected, the best fit in the 3–10 GeV band is achieved for $f_{\rm halo} = 0$, with an upper limit of $f_{\rm halo} < 0.1$ at 95% confidence level.

4.2. Quantitative Estimate of Instrumental Effects

The two independent tests described above give one confidence that instrumental effects cannot account for all the

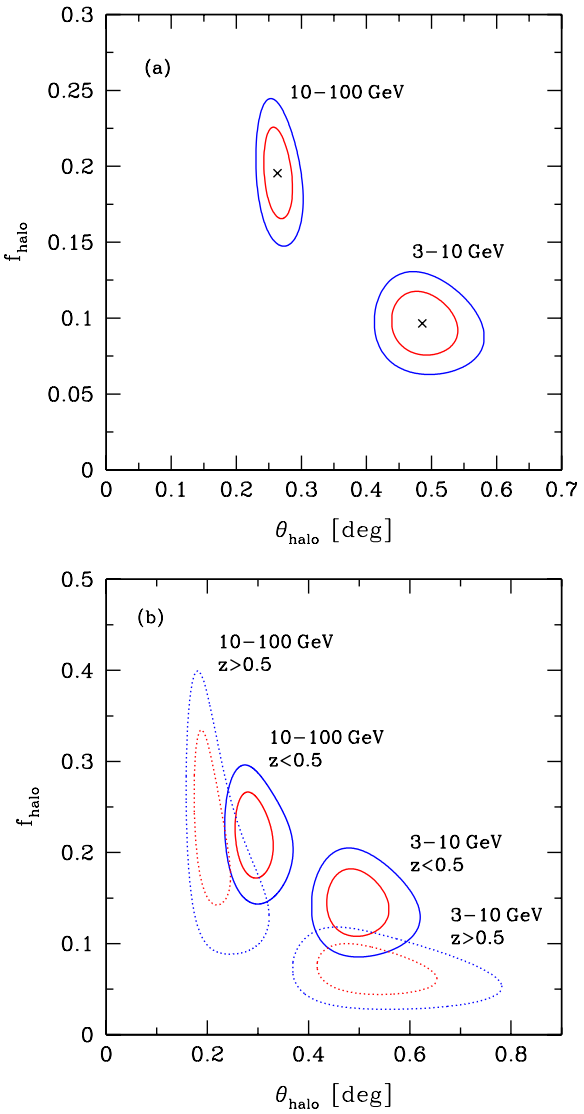

Figure 3. Allowed regions of halo size θ_{halo} and fraction of events from halo component f_{halo}. (a) Contours are at 68% and 95% confidence level obtained with the sample of 170 AGNs. The best-fit values are marked by the crosses. Lower right and upper left contours are for 3–10 GeV and 10–100 GeV, respectively. (b) Same as (a) but for 99 AGNs with known redshifts (again, right and left contours are for 3–10 GeV and 10–100 GeV, respectively). Allowed regions for nearby 57 AGNs ($z < 0.5$) are shown by solid contours, and those for distant 42 AGNs ($z > 0.5$) are by dotted contours.

(A color version of this figure is available in the online journal.)

observed halos. Neronov et al. (2010) repeated our stacking analysis and found the same anomalous excess in the 10–100 GeV band. However, they argue, "most, if not all, of this excess is due to the imperfect knowledge of the PSF for the back-converted gamma rays." This argument is based on the observation that the extent of the Crab pulsar is the same as that of the AGN, and the excess is different between front and back-converted photons. While we agree with Neronov et al. (2010) that it is good to perform other independent tests, we shall show that their arguments fail to exclude the physical halos and overturn the statistical significance of redshift and spectrum tests discussed above. To this end, we have performed an alternative analysis, using the observed Crab profile as a calibrated PSF template. This confirms our initial conclusion and demonstrates that the halos are indeed physical, at 3.5σ level. For the analysis, we mainly focus on the 3–10 GeV band, because the data

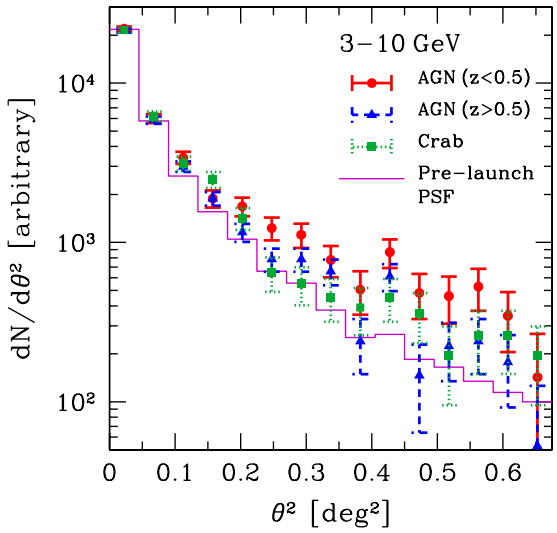

Figure 4. Surface brightness profile of AGN and the Crab pulsar as well as pre-launch PSF (for Crab) in the 3–10 GeV band. The diffuse backgrounds are subtracted. The profiles are re-scaled such that the innermost bin has the same brightness, and therefore, units in the vertical axis are arbitrary.

(A color version of this figure is available in the online journal.)

have more statistical power than in 10–100 GeV as well as the pre-launch PSF is better calibrated at lower energies (Burnett et al. 2009).

In Figure 4, we show surface brightness profiles of our nearby and distant samples of AGNs, where one can see clear difference between the two populations of AGNs. In the same figure, we also plot the profile of Crab,[5] which appears to be more consistent with the distant AGN than the nearby set. The backgrounds have been subtracted from the sources; they were estimated based on the large angular regions, where the contributions from both the point sources and halos are expected to be small. We note that the excess of AGN over Crab seen in Figure 4 was not found by Neronov et al. (2010), who analyzed the data in the 10–100 GeV band, which, as mentioned above, lacks statistical power in comparison with the 3–10 GeV band used here.

To proceed with a quantitative analysis, we use this Crab profile as a PSF model in this energy range and regard Crab statistical errors as systematic uncertainties of PSF. For example, in angular bin $\theta^2 = 0.225$–0.27 deg^2, *Fermi*-LAT received 22 photons from Crab, and the background is estimated to be 1.9. This is interpreted as 24% systematic uncertainty of PSF in this particular bin. This method is independent of our previous analysis and is free of any uncertainties related to pre-launch PSF calibration.

A possible source of additional systematic uncertainties is an energy dependence of PSF. In general, gamma-ray spectra are different between AGNs and pulsars, and so are expected PSF sizes. However, the detected spectra of both stacked AGN and Crab are well approximated by a power law with similar indices; $dN/dE_\gamma \propto E_\gamma^{-2.2}$ for nearby AGN ($z < 0.5$) and $\propto E_\gamma^{-2.4}$ for Crab, where E_γ is the gamma-ray energy. To probe the spectrum dependence of PSF even further, we compare the brightness profiles of simulated maps of nearby/hard and distant/soft AGNs. Both profiles look very similar, while the profile of hard AGNs is slightly less extended. In angular bin

[5] The Crab profile is obtained from Diffuse-class data for MET = 239557417–302034833 s.

$\theta^2 = 0.225$–0.27 deg^2, these AGN profiles differ only by 4.4%, which is negligible compared with 24% uncertainty of the Crab-based PSF due to Crab statistics. Finally, we note that the width of the PSF decreases with energy. We verified this by comparing Crab images in 3–5 GeV and 5–10 GeV bands and confirming that the former is broader than the latter. Since the spectrum of the nearby AGN is harder than that of Crab, the instrumental systematics can only make the AGN image sharper, not broader, but the opposite is inferred from Figure 4. Therefore, it is conservative to ignore the small systematic uncertainties due to spectrum dependence of PSF.

Adopting the Crab profile as a calibrated PSF, we quantitatively investigate the excess of nearby/hard AGN profiles identified at $\theta^2 \gtrsim 0.2$ deg^2 in Figure 4. The PSF and AGN profiles are normalized to each other such that they give the same brightness in the innermost angular bin, $\theta^2 < 0.045$ deg^2. The excess photon counts are $N_{\rm excess}^{(z<0.5)}(\theta^2 > 0.225\,{\rm deg}^2) = 125 \pm 30({\rm stat}) \pm 21({\rm sys})$. By taking square root of quadratic sum of the statistical and systematic errors as a total error, we find that this excess is of 3.5σ significance. For the distant/soft AGN population, on the other hand, the excess is $N_{\rm excess}^{(z>0.5)}(\theta^2 > 0.225\,{\rm deg}^2) = -5 \pm 27({\rm stat}) \pm 29({\rm sys})$, consistent with null hypothesis. Dividing $N_{\rm excess}$ by the total number of PSF counts, we obtain the values of $f_{\rm halo}$ for both AGN populations:

$$f_{\rm halo} = \begin{cases} 0.073 \pm 0.017({\rm stat}) \pm 0.012({\rm sys}), & {\rm for}\ z < 0.5, \\ -0.002 \pm 0.011({\rm stat}) \pm 0.012({\rm sys}), & {\rm for}\ z > 0.5. \end{cases} \quad (3)$$

Clearly, this conclusion using the Crab-calibrated PSF agrees with that based on the pre-launch calibration.

One can go even further and design two separate Crab-calibrated PSFs for two classes of photons, namely, those that convert in the front layer and those in the back layer of the detector. While all of these photons must be used in an analysis, allowing for the differences in PSF offers yet another opportunity to find and eliminate some unexpected instrumental effects. To this end, we introduce another statistical quantity $\delta_{\rm excess} \equiv N_{\rm excess}^{\rm front}/N_{\rm psf}^{\rm front} + N_{\rm excess}^{\rm back}/N_{\rm psf}^{\rm back}$, where all the N's with self-explanatory superscripts and subscripts refer to photon counts at $\theta^2 > 0.225$ deg^2 after the homogeneous backgrounds were subtracted. This way, we explicitly include any PSF differences between front and back-converted photons. The meaning of $\delta_{\rm excess}$ is clear: a value consistent with zero corresponds to the absence of physical halos. We obtain $\delta_{\rm excess}^{(z<0.5)} = 1.4 \pm 0.5({\rm stat}) \pm 0.2({\rm sys})$, 2.7σ away from the null hypothesis. We also find that the individual values of $\delta_{\rm excess}$ for the front and back photons are consistent with each other, within errors.

We have also performed the same analysis for 10–100 GeV. Here, we renormalized the Crab and AGN profiles using $\theta^2 < 0.025$ deg^2 bin and counted the excess photons over Crab-calibrated PSF in $\theta^2 = 0.075$–0.25 deg^2. We obtain $N_{\rm excess}^{(z<0.5)} = 19 \pm 13({\rm stat}) \pm 15({\rm sys})$ and $N_{\rm excess}^{(z>0.5)} = -3.6 \pm 9.1({\rm stat}) \pm 8.2({\rm sys})$. The excess for nearby/hard AGNs is found significant at 1σ level.

5. IMPLICATIONS FOR INTERGALACTIC MAGNETIC FIELDS

We interpret the size of the halo $\theta_{\rm halo}$ of a few tenths of degree, in terms of the secondary photon model, especially parameters of IGMF. A simple analytic model gives the following relation between these quantities (Neronov & Semikoz 2009):

$$\theta_{\rm halo} = \begin{cases} 5^\circ (1+z)^{-2} \tau^{-1} \left(\frac{E_\gamma}{10\,{\rm GeV}}\right)^{-1} \left(\frac{B_{\rm IGMF}}{10^{-15}\,{\rm G}}\right), \\ \qquad {\rm for}\ \lambda_B \gg D_e, \\ 0.^\circ 4 (1+z)^{-1/2} \tau^{-1} \left(\frac{E_\gamma}{10\,{\rm GeV}}\right)^{-3/4} \left(\frac{B_{\rm IGMF}}{10^{-15}\,{\rm G}}\right) \left(\frac{\lambda_B}{1\,{\rm kpc}}\right)^{1/2}, \\ \qquad {\rm for}\ \lambda_B \ll D_e, \end{cases} \quad (4)$$

where τ is the optical depth for the TeV photons that produce halo gamma rays, λ_B are the correlation length of IGMFs, and D_e is the energy-loss length of the electrons and positrons produced by primary TeV photons. Because the lower-energy secondary photons originate from the less energetic electrons and positrons that are deflected by larger angles in IGMF, one expects a larger halo size $\theta_{\rm halo}$ at lower energy. As for the dependence on λ_B, if it is much longer than D_e, then the charged particles can be regarded as propagating in homogeneous magnetic fields (equivalent to infinite λ_B), and therefore, the deflection angle is given by the ratio of D_e and the Larmor radius. If λ_B is much smaller than D_e, on the other hand, then the electrons and positrons propagate by random walk, with deflections proportional to $\lambda_B^{1/2}$.

The halo size for the nearby AGN sample is $\theta_{\rm halo} \approx 0.^\circ 5$–$0.^\circ 8$ (Figure 4). Assuming $\tau \sim 1$–10 and using an average redshift of the nearby AGN sample, $\langle z \rangle = 0.2$, the measured extent of the halos is consistent with $B_{\rm IGMF} \approx 10^{-15}$ G. This is the first measurement of the strength of IGMFs based on a positive detection. With the halo detection also in the 10–100 GeV band, we would be able to constrain the correlation length by investigating the energy dependence of $\theta_{\rm halo}$.

At the mean redshift of the nearby AGN sample, the observed halo size of $\sim 0.^\circ 5$–$0.^\circ 8$ corresponds to 6–10 Mpc. There are no known astrophysical sources capable of producing images of such a large size. Therefore, we conclude that the halos of the secondary photons provide the only realistic explanation of the data.

S.A. was supported by Japan Society for Promotion of Science and partially by NASA through the Fermi GI Program grant NNX09AT74G. A.K. was supported by DOE grant DE-FG03-91ER40662 and NASA ATP grant NNX08AL48G. A.K. thanks Aspen Center for Physics for hospitality.

REFERENCES

Abdo, A. A., et al. 2009, Phys. Rev. Lett., 103, 251101
Abdo, A. A., et al. 2010a, ApJS, 188, 405
Abdo, A. A., et al. 2010b, ApJ, 715, 429
Abdo, A. A., et al. 2010c, ApJ, 716, 30
Abdo, A. A., et al. 2010d, Phys. Rev. Lett., 104, 101101
Aharonian, F. A., Coppi, P. S., & Volk, H. J. 1994, ApJ, 423, L5
Aharonian, F. A., et al. 2001, A&A, 366, 746
Aleksic, J., et al. 2010, arXiv:1004.1093
Ando, S. 2004, MNRAS, 354, 414
Barrow, J. D., Ferreira, P. G., & Silk, J. 1997, Phys. Rev. Lett., 78, 3610
Baym, G., Bodeker, D., & McLerran, L. D. 1996, Phys. Rev. D, 53, 662
Burnett, T. H., Kerr, M., & Roth, M. 2009, arXiv:0912.3855
Cornwall, J. M. 1997, Phys. Rev. D, 56, 6146
Davis, A., Lilley, M., & Törnkvist, O. 1999, Phys. Rev. D, 60, 021301
Diaz-Gil, A., Garcia-Bellido, J., Garcia Perez, M., & Gonzalez-Arroyo, A. 2008, Phys. Rev. Lett., 100, 241301
Dolag, K., Kachelriess, M., Ostapchenko, S., & Tomas, R. 2009, ApJ, 703, 1078
Essey, W., Kalashev, O. E., Kusenko, A., & Beacom, J. F. 2010, Phys. Rev. Lett., 104, 141102
Essey, W., & Kusenko, A. 2010, Astropart. Phys., 33, 81
Grasso, D., & Rubinstein, H. R. 2001, Phys. Rep., 348, 163

Kronberg, P. P. 1994, Rep. Prog. Phys., 57, 325
Kulsrud, R. M., & Zweibel, E. G. 2008, Rep. Prog. Phys., 71, 0046091
Murase, K., Takahashi, K., Inoue, S., Ichiki, K., & Nagataki, S. 2008, ApJ, 686, L67
Neronov, A., & Semikoz, D. V. 2009, Phys. Rev. D, 80, 123012
Neronov, A., Semikoz, D. V., Tinyakov, P. G., & Tkachev, I. I. 2010, arXiv:1006.0164
Neronov, A., & Vovk, I. 2010, Science, 328, 73
Plaga, R. 1995, Nature, 374, 430
Strong, A. W., Moskalenko, I. V., & Reimer, O. 2004, ApJ, 613, 962
Tavecchio, F., Ghisellini, G., Foschini, L., Bonnoli, G., Ghirlanda, G., & Coppi, P. 2010, MNRAS, 406, L70
Turner, M. S., & Widrow, L. M. 1988, Phys. Rev. D, 37, 2743
Vachaspati, T. 1991, Phys. Lett. B, 265, 258
Vachaspati, T. 2001, Phys. Rev. Lett., 87, 251302
Widrow, L. M. 2002, Rev. Mod. Phys., 74, 775